AGU PUBLICATIONS

JGR

Journal of Geophysical Research: Oceans

RESEARCH ARTICLE

10.1002/2017JC013600

Key Points:

- We compute an accurate volume transport time series of the Malvinas Current at 41°S consistent with 3 in situ data sets and altimetry
- Transport maxima might result from anomalies propagating from the south above 4,000 m depths, and minima from anomalies from the overshoot
- Apart from coastal trapped waves, changes in the transport at 41°S bear no correlation with upstream conditions on the continental slope

Correspondence to:
C. Artana,
cartlod@locean-ipsl.upmc.fr

Citation:
Artana, C., Ferrari, R., Koenig, Z., Sennéchael, N., Saraceno, M., Piola, A. R., & Provost, C. (2018). Malvinas Current volume transport at 41°S: A 24 yearlong time series consistent with mooring data from 3 decades and satellite altimetry. *Journal of Geophysical Research: Oceans*, *123*, 378–398. https://doi.org/10.1002/2017JC013600

Received 2 NOV 2017
Accepted 20 DEC 2017
Accepted article online 28 DEC 2017
Published online 17 JAN 2018

© 2017. American Geophysical Union. All Rights Reserved.

Malvinas Current Volume Transport at 41°S: A 24 Yearlong Time Series Consistent With Mooring Data From 3 Decades and Satellite Altimetry

Camila Artana[1], Ramiro Ferrari[2], Zoé Koenig[1], Nathalie Sennéchael[1], Martin Saraceno[2], Alberto R. Piola[3], and Christine Provost[1]

[1]Laboratoire LOCEAN-IPSL, Sorbonne Université (UPMC, Univ. Paris 6)-CNRS-IRD-MNHN, Paris, France, [2]CIMA/CONICET-UBA and UMI IFAECI-3351, Buenos Aires, Argentina, [3]Departamento de Oceanografía, Servicio de Hidrografía Naval, DCAO/FCEN/UBA and UMI IFAECI-3351, CONICET, Buenos Aires, Argentina

Abstract We combined altimetric data and the in situ data sets from three 10 years apart mooring deployments to compute a coherent and accurate volume transport time series of the Malvinas Current (MC) at 41°S. We used a method developed in Koenig et al. (2014) and explored three types of geostrophic shear to estimate the uncertainty derived from the lack of velocity data in the upper 300 m. The mean MC transport over 24 years in the upper 1,500 m is 37.1 ± 2.6 Sv and the standard deviation 6.6 ± 1 Sv. Since 1993, annual mean transports have varied from 32 to 41 Sv and the three in situ records corresponded to low annual mean transports. The MC transport time series is not stationary, its spectral content evolves with time showing significant energy at the 30–110 days, semiannual and annual period. The distribution of the MC volume transport anomalies is asymmetric, negatively skewed with larger negative anomalies than positive anomalies. Several transport maxima appear to result from cyclonic eddies that propagate northwestward following the 4,000–5,000 m isobaths and locally reinforce the circulation on the slope when they reach 41°S. During transport maxima, the northernmost extension of the Subantarctic Front (SAF) remains at its mean location (39.5°S). During minima, the SAF migrates southward of 41°S as positive anomalies shed by the Brazil Current overshoot moves westward onto the slope. Apart from continental trapped waves, changes in the MC volume transport at 41°S show no correlation with upstream conditions on the continental slope.

1. Introduction

The Malvinas Current (MC) is a cold and nutrient-rich current that originates in Drake Passage, where the steep topography forces the northernmost branch of the Antarctic Circumpolar Current (ACC), the Subantarctic Front (SAF), to turn northward and enter into the western Argentine Basin. The MC, which follows the SAF (Figure 1a), is an intense current which penetrates northward along the Patagonian shelf break along the 1,000–2,000 m isobaths. The MC carries fresh Subantarctic waters that enrich the Patagonian shelf with nutrients and sustain the high productivity of this region (Acha et al., 2004; Carranza et al., 2017; Romero et al., 2006; Valla & Piola, 2015). At 39°S, the MC encounters the warm-salty Brazil Current (BC) which follows the Brazil Current Front (BCF, Figure 1a). After the collision, both currents separate from the continental slope and veer offshore. The BC overshoots southward to about 45°S (Figure 1a). The SAF describes a sharp cyclonic loop toward the south reaching the southern edge of the Argentine Basin at 49°W–49°S where it merges with the Polar Front (PF) of the ACC (Figure 1a). The return flow associated with the southward path of the SAF is called the Malvinas Return Current (MRC; Piola et al., 2013).

Although the MC is an emanation of the ACC, the link between MC variations and the ACC is not clear. The lack of correlation between the northward penetration of the MC and wind forced pulses of the ACC suggested that the MC variations are uncoupled from the ACC (Garzoli & Giulivi, 1994). In contrast to the ACC in Drake Passage, the MC shows a modest eddy kinetic energy (~150 $cm^2\ s^{-2}$) as the topographic barriers of the North Scotia Ridge and the Malvinas Plateau filter and reduce the mesoscale activity (>1,000 $cm^2\ s^{-2}$) coming from the south (Artana et al., 2016; Figure 1b). Occasionally, intense mesoscale anticyclonic anomalies from the Argentine Abyssal plain (Figure 1b) propagate westward along the Malvinas Escarpment at

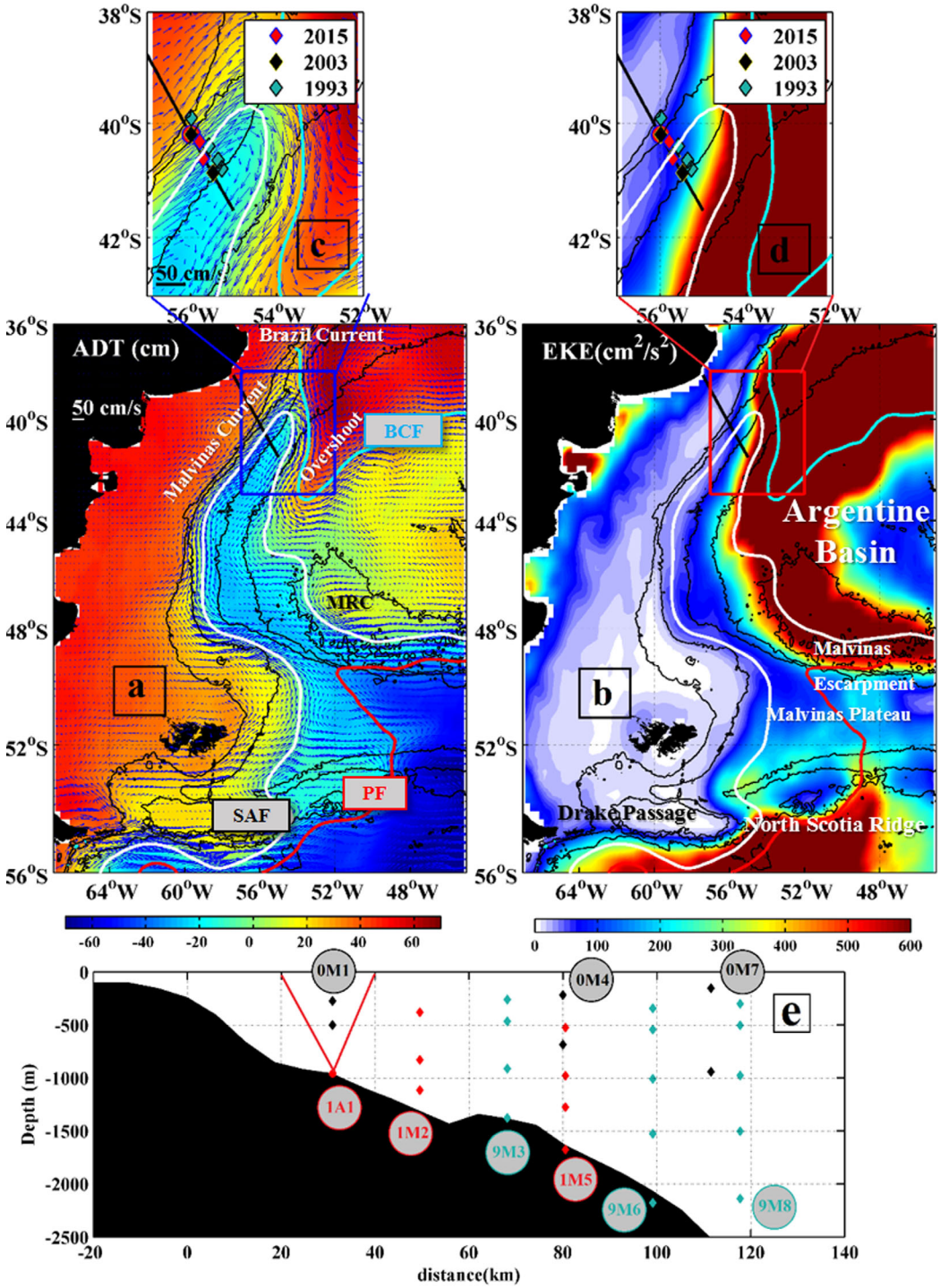

Figure 1. (a–c) Mean absolute dynamic topography (ADT) (in cm) and (b–d) eddy kinetic energy (EKE) (in cm^2/s^2) from 24 years (1993–2016) of satellite altimetric data. Bottom topography isobaths (from Smith & Sandwell, 1994) correspond to 6,000, 5,000, 3,000, 3,100, 2,000, 2,500, 1,000, and 300 m. The white, cyan, and red contours represent the mean position of the Subantarctic Front (SAF), Brazil Current Front (BCF), and Polar Front (PF) and are respectively defined as contours of ADT values of −5, +30, and −40 cm as in Ferrari et al. (2017). The black line indicates the position of Jason track #26. The mooring data that are not aligned on the track (9M3, 9M6, and 9M8) are attributed to the nearest point on the track with the same bottom depth. (e) Vertical distribution of the current meter moorings and ADCP from 2014 to 2015 (red diamonds), 2001 to 2003 (black diamonds), and 1993 to 1995 (green diamonds).

48.5°S and cut a large fraction of the MC from its source (Artana et al., 2016). These blocking events are short lived (from 10 to 35 days) and the MC downstream does not collapse rather becomes the western boundary of a robust recirculating cyclonic cell (Artana et al., 2016).

Current meter mooring data in the MC have been obtained at approximately 41°S along Jason track #26 (black line in Figure 1a) near the Confluence with the BC at three different times: in 1993–1995 (Vivier & Provost, 1999a, hereafter VP99a), 2001–2003 (Spadone & Provost, 2009, hereafter SP09), and 2014–2015 (Ferrari et al., 2017; Figures 1c–1e). At 41°S, the MC has mainly a barotropic equivalent structure due to the weak stratification and the steep topography and is made of one single core in contrast to the several narrow jets observed south of 42°S (VP99a; Piola et al., 2013). A method, so called classical method hereafter, was designed in 1999 to obtain a reliable MC transport time series of the upper 1,500 m combining satellite altimetric data and in situ measurements (Vivier & Provost, 1999b; hereafter VP99b). Based on this method, the intraseasonal variability of the MC was examined in a 5 yearlong transport time series (Vivier et al., 2001). The coherence between a variability of 70 day periodicity and the bottom-pressure variability observed in the northern Drake Passage with a time lag shorter than 20 days was associated with baroclinic shelf waves propagating along the edge of the Patagonian shelf at a speed between 2.5 and 3 m/s. Interannual variations were examined in a 14 yearlong (1993–2007) MC transport time series (upper 1,500 m) also constructed with the classical method using in situ data from the first two deployments (SP09). A change in the spectral characteristics of the transport variations was observed: shorter periods (50–90 days and the semi-annual period) dominated from 1993 to 1997 while a strong annual period dominated from 2001 to 2005. This change was accompanied by a southward migration of the Brazil Current Front, which made difficult to tell apart intrinsic variations of the MC from mesoscale perturbations due to the proximity of the Brazil-Malvinas Confluence to the moorings (Figures 1c and 1d; SP09).

The main objective of this paper is to produce a 24 yearlong volume transport time series of the MC at 41°S across Jason satellite ground track #26 (upper 1,500 m) to study variations of the MC. We aim at combining altimetric data and the in situ data sets from the three periods 1993–1995, 2001–2003, and 2014–2015 to compute a coherent and accurate transport time series.

The paper is organized as follows. Data and methods are presented in section 2. Once volume transport time series are produced and their uncertainties assessed, the general statistics and time scales of variations are described in section 3. Section 4 investigates variations of the MC volume transport, documents extrema and examines statistical relationships between variations of the MC volume transport and sea level anomaly over the Southwest Atlantic Ocean at different lags. Finally, a summary and discussion of the main results of this study are presented in section 5.

2. Data and Methods

2.1. Data

2.1.1. Mooring Data

The current meter data are from moorings deployed in 1993–1995 (9M3, 9M6, and 9M8, green in Figure 1e and Table 1; Provost et al., 2017a), 2001–2003 (0M1, 0M4, and 0M7, in black Figure 1e; Provost et al., 2017b), and 2014–2015 (1A1, 1M2, and 1M5, in red in Figure 1e; Saraceno et al., 2017). Altogether the moorings from the three measurement periods are complementary and document the flow on the slope: data from the first deployment (green diamonds in Figure 1e) provide information on the outer slope (at depth $>$ 1,500 m as a mooring placed on the 1,000 m isobath was lost) while the recent data set (red diamonds in Figure 1e), including an Acoustic Doppler Current Profiler (ADCP) data moored on the 1,000 m isobaths (1A1 mooring), samples the upper slope. The data set from 2001 to 2003 comprises three moorings carrying only two instruments each and allows comparisons between periods (black diamonds in Figure 1e).

Some moorings experienced drawdowns during strong current pulses. The standard deviation of the vertical displacement is 30–60 m for the upper instruments (Table 1). As the velocity is not sufficiently densely sampled on the vertical axis to guarantee accurate corrections, the velocity data were not corrected for mooring motion and the corresponding statistics refer to the mean depth of the instruments. As shown in VP99a, mooring motions may lead to an underestimation of the mean velocity by 2% and 20% of the velocity variance. All the current meter data were low-pass filtered with a Loess filter with a cutoff period of 50 h (to remove tidal and inertial variability) and subsampled at a daily rate.

Table 1
Description of Moorings

	Lat.	Lon.	Bottom depth (m)	Current meter type	Record length (days)	Mean pressure (dbar)	Std pressure (dbar)
0M1	−40.202	−55.978	1,010	VACM	416	274	33
				VACM	433	502	18
1A1	−40.201	−55.975	1,030	ADCP	336	1,007	0.4
1M2	−40.325	−55.780	1,319	Aquadopp	337	380	46
				Aquadopp	337	829	20
				Aquadopp	337	1,116	12
9M3	−40.406	−57.571	1,507	VACM	386	261	54
				VACM	179	467	53
				VACM	512	912	25
				VACM	512	1,377	3
0M4	−40.582	−55.678	1,510	VACM	433	217	44
				VACM	426	217	28
1M5	−40.630	−55.699	1,945	Aquadopp	336	524	29
				Aquadopp	336	978	11
				Aquadopp	328	1,275	6
				Aquadopp	336	1,677	1
9M6	−40.654	−55.353	2,536	VACM	540	342	42
				VACM	512	544	41
				VACM	512	1,009	28
				VACM	512	1,527	14
				VACM	512	2,177	2
0M7	−40.877	−55.475	2,536	VACM	179	153	62
				VACM	433	942	51
9M8	−40.808	−55.269	3,043	VACM	546	300	45
				VACM	546	504	43
				VACM	513	975	35
				VACM	88	1,502	28
				VACM	213	2,134	11
				VACM	149	2,905	3

Note. Mooring position, bottom depth, current meter type, record length, mean pressure, and standard deviation of the pressure. VACM stands for vector averaging current meter (Aandera RCM7 and 8), Aquadopp is an acoustic single point current meter (Nortek), ADCP is an acoustic Doppler profiler (75 kHz RDI).

2.1.2. Satellite Data

We used DUACS delayed time altimeter gridded products (Pujol et al, 2016) produced as part of the Copernicus Marine and Environment Monitoring Service (CMEMS) (http://marine.copernicus.eu/). We used the "Updated" product, which includes data from all available altimeters at any given time. The altimetric product has a spatial resolution of 1/4° on a Mercator grid and a daily sampling. The multisatellite gridded product is based on a space-time interpolation and its actual temporal resolution is not 1 day, rather 20 days (Pujol et al., 2016). The products comprise sea level anomaly (SLA), absolute dynamic topography (ADT), surface geostrophic velocities, and surface geostrophic velocity anomalies. The SLA product is computed relative to the mean dynamic topography (MDT) from CNES-CLS13 (Rio et al., 2013), which is the mean of the sea surface height above the geoid over the period 1993–2012, and is obtained from gravity and altimetry satellite data and in situ oceanic observations. The gridded altimetric products were linearly interpolated onto the 160 km-long portion of Jason satellite ground track #26 with a spacing of 7 km (Figure 1). The correlation coefficients between the 20 day low-passed filtered cross-track velocities at each mooring upper level and altimetry-derived surface geostrophic velocities interpolated at the mooring position are larger than 0.8 for the three data sets (Ferrari et al., 2017). Gridded altimetry products are preferred to the near 10 day repeat cycle along-track product as they compare better with in situ data (Ferrari et al., 2017).

2.2. Methods to Compute Volume Transport Time Series

We use two different methods to compute a MC transport time series combining altimetry (1993–2016) and in situ data. We implement the classic transport estimation method used in VP99b and SP09, and a new look-up table (LUT) method developed by Koenig et al. (2014) to estimate the ACC volume transport

through the Drake Passage. We focus on the geostrophic volume transport and ignore Ekman transport. As upper level current meters are below 300 m depth, the lack of information on the velocity shear in the upper 300 m is a source of uncertainty. We use different types of upper velocity profiles to test the sensitivity of the volume transport to the geostrophic shear in the upper 300 m of the water column.

2.2.1. Classic Transport Estimation Method

The classic transport estimation method (VP99b, SP09) consists in deriving the cross-track velocity field as follows:

$$V(x,z,t)=V_m(x,z)+A(x,z)\times V'(x,0,t) \tag{1}$$

where x is the along-track coordinate with $x=0$ above the 300 m isobath, $V_m(x,z)$ is the time-averaged velocity field across the section estimated from the observations, A(x,z) a function describing the vertical structure of the cross-track flow, and $V'(x,0,t)$ is the cross-track surface geostrophic velocity anomaly derived from altimetry. A(x,z) is obtained from the velocity correlation coefficients between the uppermost current meter and the underlying instruments. The correlation coefficient is extrapolated to the surface through a linear extrapolation, then it is normalized to unity at the surface and mapped over the section. The MC cross-section volume transport is then obtained by integrating the velocity field at each time step (1 day) over the upper 1,500 m. Only positive velocities (equatorward flow) are considered.

SP09 observed that the in situ velocity statistics from periods 1993 to 1995 and 2001 to 2003 were coherent, and combined current meters data from both periods (9M3, 9M6, and 9M8 for 1993–1995; 0M1, 0M4, and 0M7 for 2001–2003) to construct $V_m(x,z)$ and A(x,z). Information from surface drifters was used to estimate the mean surface velocity $V_m(x,0)$. The altimetric product used by SP09 differs from the current altimetric product. They used along-track SLA referred to the period 1993–1999 with a spatial sampling of 7 km (the data being low-passed filtered with a 70 km cutoff wavelength) and a temporal sampling of 9.916 days. We checked that over the period analyzed by SP09 (1993–2007), the transport time series computed using SP09's $V_m(x,z)$ and A(x,z) and the current gridded surface geostrophic velocity anomalies (referred to 1993–2012) was consistent with the SP09 transport time series (same mean, same standard deviation, and correlation larger than 0.99). The consistency between both altimetric products allows the computation of a 24 yearlong transport time series using SP09's $V_m(x,z)$ and A(x,z), and the current gridded surface geostrophic velocity anomalies.

2.2.2. Look-Up Table Method

The new method developed by Koenig et al. (2014, 2016) involves a "look-up table" (LUT) that allows for time-variable transfer function of the vertical structure. The LUT method consists in calculating the velocity profiles at each point x along the track and at each time t as function of the surface velocity, as follows:

$$V(x,z,t)=B(x,z,V(x,0,t)),\ \text{with}\ V(x,0,t)=V_s(x)+V'(x,0,t) \tag{2}$$

where B is a function (named look-up table B) that depends on the along-track position x, the depth z, and the surface velocity V(x,0,t). The surface velocity V(x,0,t) is the sum of a time-averaged surface velocity $V_s(x)$ and the surface velocity anomaly $V'(x,0,t)$ derived from satellite altimetry. The method requires a good knowledge of the vertical velocity structure and an accurate time-averaged surface velocity Vs(x).

The methodology (schematized in Figure 2) implies three major steps:

A. the construction of a look-up table $B(N_x,N_z,N_v)$;
B. the estimation of a mean surface velocity $V_s(x)$; and
C. the validation with a posteriori comparison of reconstructed velocities with 20 day low-pass filtered in situ velocities (section 2.3).

The look-up table of velocity profiles is built using the current meter data from periods 1993 to 1995 and 2014 to 2015. The lower vertical resolution current meter data from 2001 to 2003 are used as independent data to check the consistency of the method.

Cross-track velocity profiles from each mooring (velocities at three or four depths in general except for the ADCP with 31 levels, one level every 25 m) are binned into different classes according to the upper current meter velocity. The upper cross-track velocities are sorted out into 11 bins between −35 and 60 cm/s. Then, the affiliation of the velocity of the underlying current meters to a class is determined by the uppermost current meter velocity range (step 1 in Figure 2). We then average the velocity values of each bin at each

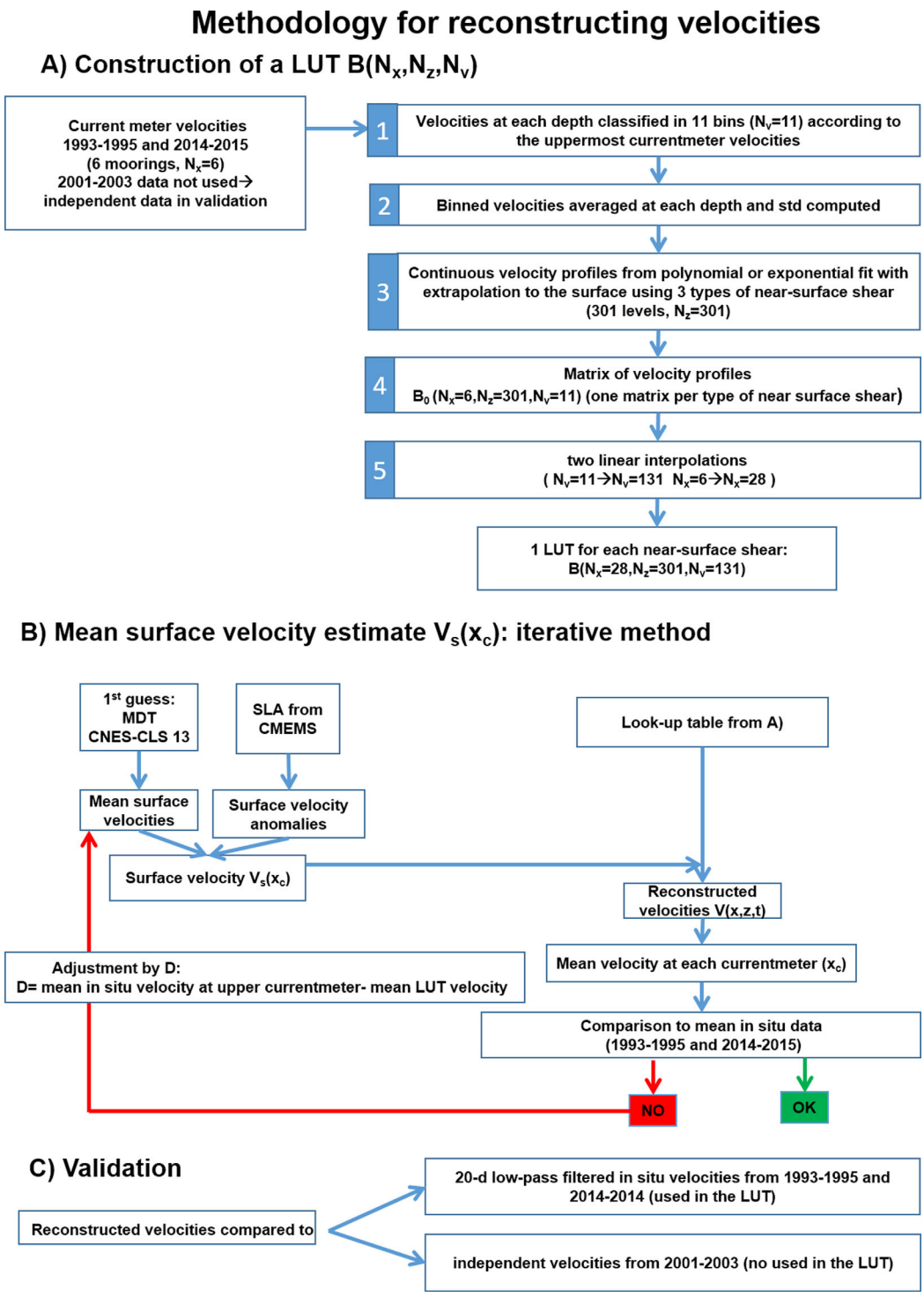

Figure 2. Schematics of the methodology used to obtain the cross-track reconstructed velocities ((a) construction of the look-up table (LUT), (b) mean surface velocity estimate, and (c) validation). CMEMS, Copernicus Marine and Environment Monitoring Service; MDT, mean dynamic topography; SLA, sea level anomaly.

depth and compute the standard deviation (step 2 in Figure 2 and dots and bars in Figure 3). An exponential or polynomial fit (first or second order) is applied to the means in each class to obtain continuous vertical profiles (step 3 in Figure 2 and thick lines in Figure 3). Each mooring presents one or two dominant profiles with a percentage of occurrences larger than 20% (Figure 3, orange and red profiles). As the MC

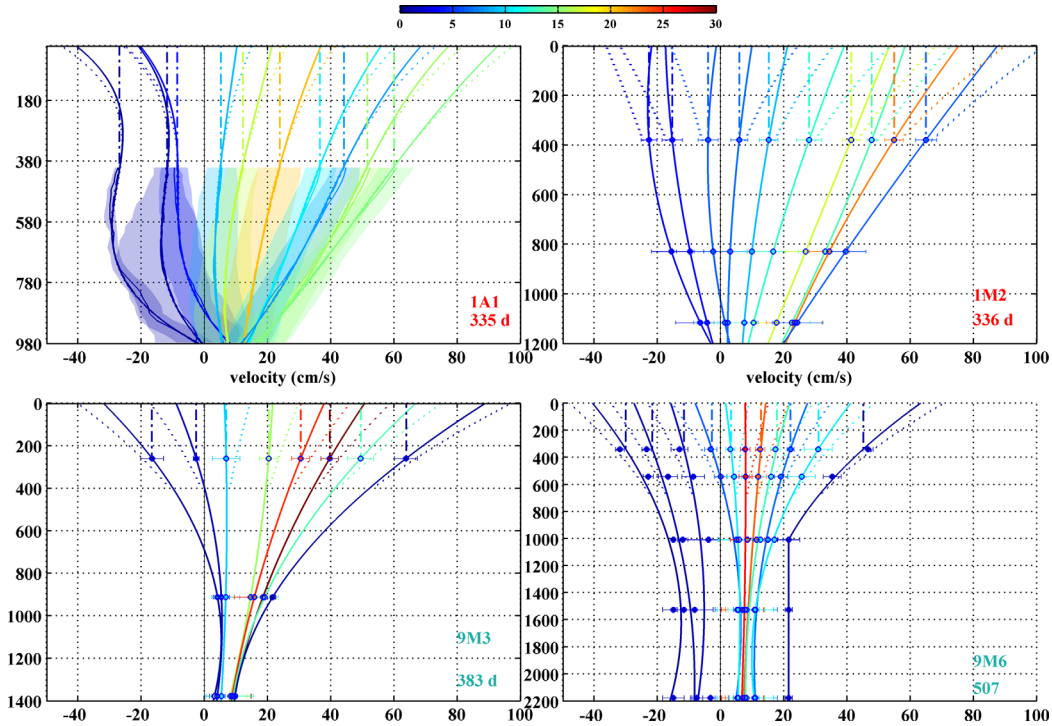

Figure 3. Velocity profiles at the mooring position classified as function of their upper level velocity for moorings 1A1, 1M2, 9M3, and 9M6. The *x* axis is the velocity (in cm/s, positive is equatorward) and the *y* axis the depth (in meters). Note that depth scale varies from one figure to the other. The dots (thin lines) indicate the mean velocity of the current meter (ADCP, mooring 1A1) for a given surface velocity range. At each depth, the error bars (shaded areas) represent the standard deviation for a given surface velocity range computed from current meters (ADCP). The velocity profile between the upper level observation and the surface is interpolated in three ways: zero shear (dashed-dotted line), polynomial fit (fitted shear thick line), and large near-surface shear (dotted line). Colors represent the percentage of occurrence of each profile.

flows equatorward, the dominant profile is always positive and profiles belonging to negative velocity values have a low percentage of occurrence (less than 5%). The positive velocity profiles and the standard deviation associated to positive bins reflect the barotropic equivalent nature of the MC (VP99a). Only positive profiles are used in the computation of the MC volume transport time series.

There are no current meter data near the surface, so the information on the shear between the uppermost instrument (about 300 m) and the surface is provided by the polynomial fit. To assess the sensitivity of the method to the geostrophic near-surface shear, we use two other shear structures apart from the structure provided by the fit (referred to as the fitted near-surface shear structure, thick lines in Figure 3): one assuming no shear between the uppermost current meter and the surface (zero near-surface shear structure, dashed-dotted lines in Figure 3), and the other increasing the shear by adding 10 cm/s to the surface velocity amplitude obtained with the fitted shear (large near-surface shear structure, dotted lines in Figure 3).

For each type of geostrophic near-surface shear, we pool all the velocity profiles in a matrix (step 4 in Figure 2) $B_0(N_x,N_z,N_v)$, with N_x the number of mooring positions along the track ($N_x = 6$), N_z the number of vertical levels ($N_z = 301$ corresponding to 10 m resolution from the surface to 3,000 m), and N_v the number of surface velocity bins. Two linear interpolations are performed to extend the look-up table. First, velocity values are linearly interpolated each 1 cm/s between -50 and 80 cm/s. We then obtain a matrix $B_1(N_x,N_z,N_v)$, where now $N_x = 6$, $N_z = 301$, and $N_v = 131$. Then, the distance x along the track is linearly interpolated to a 7 km resolution (step 5 in Figure 2). Thus, for each type of geostrophic near-surface shear, we obtain a final look-up table of velocity profiles B(28,301,131). The linear interpolation is consistent with the barotropic equivalent nature of the MC (VP99a).

The mean cross-track surface velocity $V_s(x)$ (equation (2)) is adjusted at each current meter position (x_c) using the look-up table B and an iterative method described in Koenig et al. (2014) and recalled in Figure 2 (step B). The initial guess for $V_s(x_c)$ is the mean surface geostrophic velocity (MSGV) from the CLS-CNES13

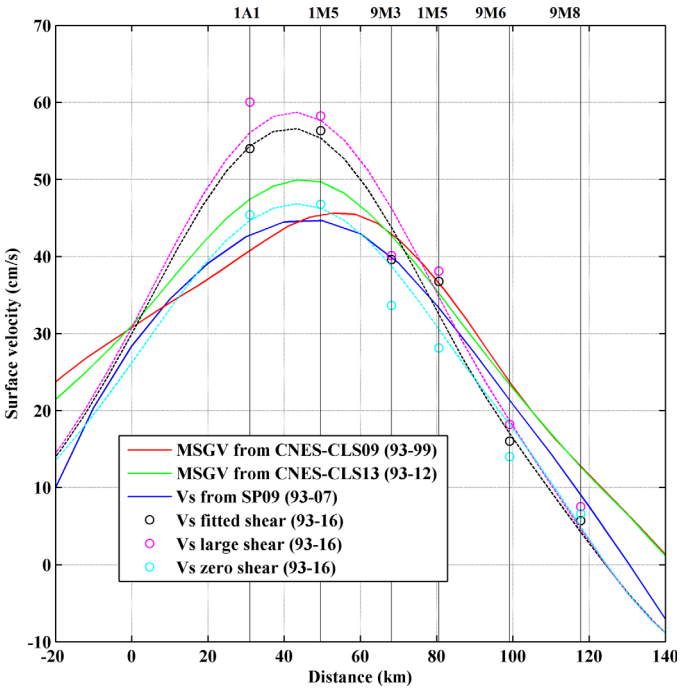

Figure 4. Across-track mean surface geostrophic velocity (MSGV) from CNES-CLS09 mean dynamic topography (MDT) in red, from CNES-CLS13 MDT in green, and from SP09 in blue. Colored dots represent the mean surface geostrophic velocity for each type of near-surface shear at the mooring position resulting from the iterative method (cf., Figure 2). The dashed lines are the new mean surface velocity profiles for each type of near-surface shear.

mean dynamic topography (Rio et al., 2013). The reconstructed velocities $V(x_c,z,t)$ using surface velocities $V(x_c,0,t)$ (the sum of the mean cross-track velocities $V_s(x_c)$ and cross-track velocity anomalies $V'(x_c,0,t)$ deduced from SLA) and the LUT are compared with the in situ velocities. The mean surface cross-track velocity $V_s(x_c)$ is corrected by the difference between the mean in situ velocity at the uppermost current meter and the estimated velocities at the same depth (D). The process is repeated, that is $V_s(x_c)$ adjusted until D is less than 0.5 cm/s. This successive error/correction is applied iteratively at each mooring, until the criterion ($D < 0.5$ cm/s) is satisfied. Four iterations are found necessary to produce a surface velocity $V_s(x_c)$ consistent with the in situ data and the look-up table. The final mean surface velocity values at each mooring location and for each type of shear (dots in Figure 4) are fitted with a Gaussian function to obtain $V_s(x)$ along track #26 (dashed lines in Figure 4).

Six different mean surface velocity estimates are shown in Figure 4 (SP09, CNES-CLS09, CNES-CLS13, and the 3 LUT with different near-surface shears). Note that they correspond to means over different periods (see Figure 4). All the adjusted estimates indicate a maximum velocity at the same location (along-track distance 40 km) except for the MSGV from CNES-CLS09 where the maximum is further offshore by 20 km. The velocity maximum varies over a range of 14 cm/s, from 45 cm/s (SP09) to 59 cm/s for the LUT estimate with large shear. The LUT method provides a velocity maximum of 47 cm/s for the extreme case of zero shear and similar values of 57 and 59 cm/s for the fitted and large shears. The mean surface velocity estimate from LUT covers a wide range, stressing the importance of near-surface shear.

2.3. Assessment of the Reconstructed Velocities Comparing to Mooring Data

Cross-track velocities along ground track #26 corresponding to the current meter records (location and time) are reconstructed using the classic method (with the Vm(x,z) and A(x,z) from SP09) and the LUT method with the three different geostrophic near-surface shears. To validate the method, the reconstructed velocities are compared to 20 day low-pass filtered in situ velocities from each mooring period (step C in Figure 2). Velocity statistics for the in situ data from the first and last mooring deployments (20 day low-pass filtered) and the four reconstructed velocities are presented in Table 2. In general, reconstructed means at each current meter depth are within 1 cm/s of the observed values except those reconstructed from the classical method using SP09 parameters (Vm and A) where differences exceed 10 cm/s at 1A1 and 1M1. Note that these current meter data (1A1 and 1M1) are from the recent deployment (2014–2015) and consequently, their information is not included in calculating Vm(x,z) and A(x,z) in SP09 while it is used in the LUT. The correlations between the four reconstructed velocities and the 20 day low-pass filtered in situ data are similar and in general larger than 0.7 except near the bottom. The agreement between reconstructed and in situ velocities is particularly satisfying in the core of the MC at 1A1and 1M1. In general, the standard deviation of the reconstructed velocities is smaller than that of the 20 day low-pass filtered in situ data (Table 2). The variance reduction is likely a consequence of smoothing of the altimeter data. The satellite velocity anomaly is smoothed while computing the gridded product, whereas in situ data are point measurements (Ferrari et al., 2017).

To check the consistency of the LUT-reconstructed velocities we computed the means and standard deviations at the position of moorings from period 2001 to 2003. Recall that the 2001–2003 data were not used to estimate matrix B in the LUT method. Correlations between reconstructed and in situ velocities vary between 0.7 and 0.9. The LUT method with any of the three near-surface shears performs better than SP09 in terms of means and root-mean-square error (not shown). Therefore, the LUT-reconstructed velocities are very consistent with the in situ data from any period and are preferred to the velocities derived from SP09.

Table 2
Statistics of the In Situ and Reconstructed Velocities

		In situ		LUT fitted shear			LUT large shear			LUT zero shear			Classic method			
Current meter (isobaths)	Depth (m)	Mean (cm/s)	Std (cm/s)	Δ mean (cm/s)	Std (cm/s)	RMSE (cm/s)	Δ mean (cm/s)	Std (cm/s)	RMSE (cm/s)	Δ mean (cm/s)	Std (cm/s)	RMSE (cm/s)	Δ mean (cm/s)	Std (cm/s)	RMSE (cm/s)	r
1A1 (1,030 m)	400	31.3	19.3	−0.2	14.8	9.7	−0.1	11.7	10.4	0.0	17.2	8.9	−12.7	15.1	15.9	0.9
	600	22.7	14.7	−1.2	13.5	10.0	−1.5	9.0	10.9	0.7	13.4	8.9	−11.8	14.1	15.1	0.9
	880	14.7	8.1	0.1	9.7	5.6	−0.8	47	8.7	0.5	7.0	5.1	−6.2	10.1	8.9	0.8
1M2 (1,319 m)	380	33.3	21.2	−0.2	14.9	9.5	−0.1	14.7	9.7	0.0	19.0	8.5	−11.4	15.8	14.6	0.9
	829	21.2	14.1	−0.4	10.0	7.0	−1.6	9.6	7.4	0.5	12.2	6.7	−7.8	12.2	10.3	0.9
	1,116	14.2	9.8	0.0	6.9	6.3	−0.4	6.4	7.3	0.0	7.9	6.5	−6.1	9.6	9.2	0.7
9M3 (1,507 m)	261	31.7	11.4	0.5	9.4	7.7	0.4	7.8	6.2	0.0	9.4	5.9	−0.1	8.4	6.1	0.8
	912	16.1	4.7	1.7	5.6	4.3	0.9	4.1	3.6	4.7	6.0	6.5	2.3	2.3	4.9	0.7
	1,377	7.6	2.5	2.0	3.1	3.9	0.5	1.8	2.6	3.8	2.7	4.9	4.0	4.0	4.9	0.3
1M5 (1,945 m)	524	26.3	14.8	−0.5	9.4	7.8	−0.2	9.4	7.8	0.0	13.7	6.9	−0.3	10.8	7.2	0.9
	978	19.1	10.2	−1.4	5.6	9.7	−2.0	5.6	13.4	−1.2	8.2	11.8	−3.9	8.4	13.8	0.8
	1,275	11.7	7.9	−0.8	3.1	9.4	−0.4	3.2	9.8	0.7	4.7	7.6	0.7	5.5	17.2	0.6
9M6 (2,200 m)	342	11.5	9.0	0.5	6.5	6.2	0.3	6.0	6.4	0.0	8.9	6.7	2.0	7.4	6.6	0.7
	544	10.9	7.2	0.3	5.4	5.0	−0.9	5.0	5.4	−0.2	7.3	5.4	1.3	6.7	5.5	0.7
	1,009	9.9	5.7	−0.4	3.4	5.2	−1.6	2.3	6.5	−0.7	4.5	5.7	0.4	5.3	6.4	0.3
9M8 (3,040 m)	300	3.8	8.9	0.3	7.5	5.8	0.4	6.6	5.7	0.0	9.7	6.3	−1.0	8.6	6.0	0.8
	504	3.8	7.2	0.9	6.2	5.2	0.0	5.0	5.0	0.4	8.4	5.8	1.1	10.3	5.7	0.7
	975	4.7	5.1	0.5	3.7	4.3	−0.8	2.1	5.0	−0.2	5.9	5.2	−1.2	6.0	5.2	0.6

Note. Mean and standard deviation of in situ velocities for all the current meter records used in the LUT (1993–1995 and 2014–2015). Mean differences, root-mean-square difference and the correlation coefficient (r) between in situ velocities and reconstructed velocities. Standard deviation of the reconstructed velocity for each type of LUT and for the classic method using SP09 parameters (V_m and A).

2.4. LUT-Reconstructed Velocities in the Framework of the "Classical Method"

To put the LUT-reconstructed velocities V(x,z,t) in the framework of the "classical method," we computed the mean cross-track velocity Vm(x,z) and the time-dependent vertical structure A(x,z,t) from equation (3):

$$A(x,z,t) = (V(x,z,t) - V_m(x,z))/V'(x,0,t) \tag{3}$$

where V′(x,0,t) is the surface cross-track velocity anomalies computed from SLA.

The mean cross-track velocities $V_m(x,z)$ from the three LUT estimates (Figures 5a–5c) present larger values than the $V_m(x,z)$ from SP09 in the upper 500 m in the core of the MC (Figure 5d). The zero near-surface shear provides the lowest mean near-surface velocities of the three LUT estimates. The mean velocity difference between the surface and 250 m depth for the fitted near-surface shear and the large near-surface shear shows large values over the upper slope and decreases further offshore (Figure 5e). The mean velocity difference between the surface and 250 m shows a maximum located around the 30 km of 13 cm/s for the large near-surface shear and 10 cm/s for the fitted near-surface shear. SP09 mean velocity difference between the surface and 250 m decreases monotonically offshore from 12 cm/s at km 0 to 0 cm/s at km 140. The LUT method allows for negative upper water column shears on the offshore part of the section, which is expected when the Brazil overshoot migrates westward (VP99a). The standard deviation in the velocity difference between the surface and 250 m for the fitted and large shear exceeds 6 cm/s in the offshore part of the section. In contrast, the standard deviation in SP09 is unrealistically small (less than 2 cm/s) all along the section (Figure 5e).

The mean vertical structures A(x,z) deduced from averaging A(x,z,t) from (3) over time for each LUT are quite different in the upper layer as expected from the different shears (Figures 6a–6c). The zero-shear LUT-derived A(x,z) features values in excess of 0.9 in the upper 700 m (Figure 5b). The three LUT-derived A(x,z) show a 0.3 isoline at shallower depth (between 1,000 and 1,500 m) than observed in the SP09 A(x,z) (Figure 6). The SP09 A(x,z) is merely extrapolated from the in situ data (Figure 6d), whereas the three LUT A (x,z) take into account altimetric data (Figures 6a–6c). The three LUT estimates indicate a shallower level (1,000 m) for the 0.3 isoline at km 30 than at km 60 which is information provided by the ADCP not available in SP09. We will see in the following sections that these differences in the mean and vertical structure somehow compensate along the section as the resulting transport time series are quite similar to each other.

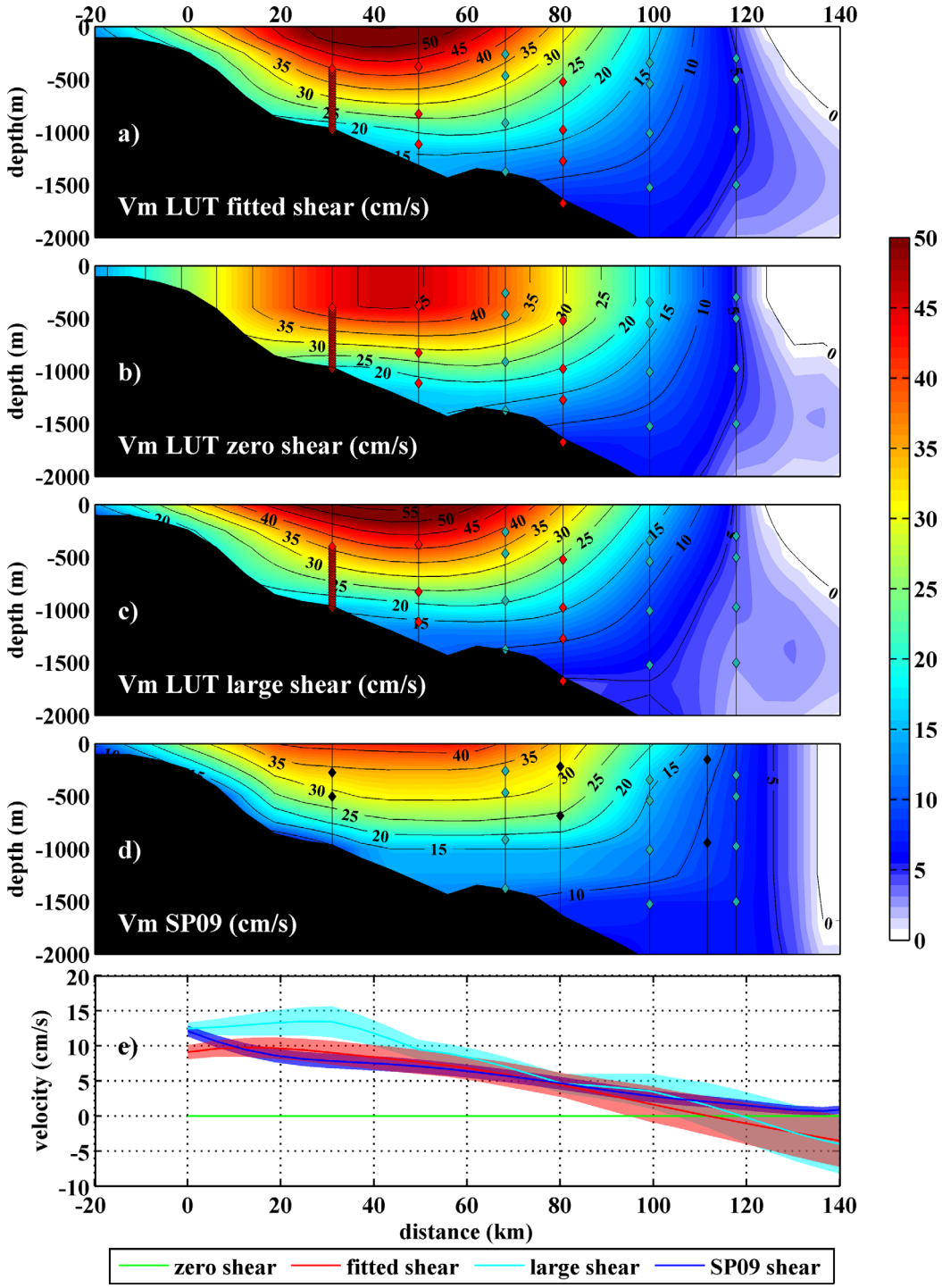

Figure 5. Mean velocity field across the section in cm/s deduced from the look-up table (LUT) for each type of shear ((a) fitted near-surface shear, (b) zero near-surface shear, and (c) large near-surface shear) and (d) for SP09. Mooring position is indicated with vertical lines. Red diamonds: moorings from 2014 to 2015. Black diamonds: moorings from 2001 to 2003. Green diamonds: moorings from 1993 to 1995. (e) Mean velocity difference between the surface and 250 m for each type of shear and for SP09. Shaded areas represent standard deviation.

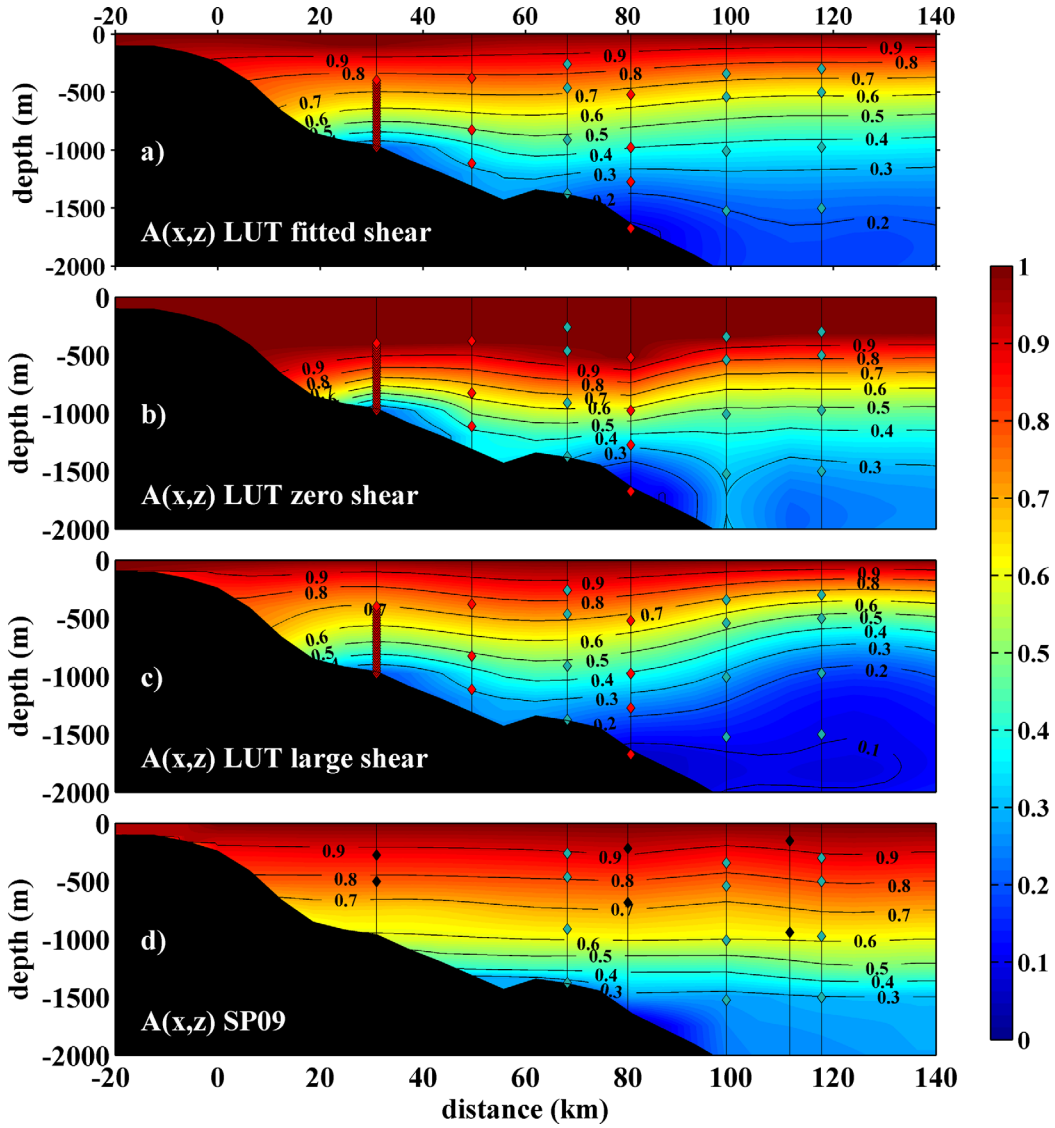

Figure 6. Function A(x,z) obtained for each type of shear ((a) fitted near-surface shear, (b) zero near-surface shear, and (c) large near-surface shear) and (d) from SP09. Mooring position is indicated with vertical lines. Red diamonds: moorings from 2014 to 2015. Black diamonds: moorings from 2001 to 2003. Green diamonds: moorings from 1993 to 1995.

3. MC Volume Transport Time Series: Assessment and General Statistics

3.1. Assessment of the Different Transport Time Series

Twenty-four yearlong volume transport time series of the MC above 1,500 m were computed from the positive (equatorward) velocities derived from the four different methods (SP09 and the three LUT) with a daily sampling. Because the altimetry product is based on a space-time interpolation, the transport time series cannot resolve variations with periods shorter than 20 days. The four transport time series are highly correlated with each other ($r > 0.99$), and only one transport time series is shown (Figure 7). We choose the LUT transport computed with fitted near-surface shear as justified below. The means and standard deviations of the 24 yearlong transport time series do differ however (Table 3). As expected from the mean velocity sections (Figure 5), SP09 transport has the smallest mean (33.2 Sv). The means of the LUT-derived transports are 34.6 Sv (large shear), 37.1 Sv (fitted shear), and 39.8 Sv (zero shear). Standard deviations of the volume transports range from 6.0 to 7.9 Sv (Table 3). The standard deviation is largest for the LUT method with a zero near-surface shear and smallest for the large shear.

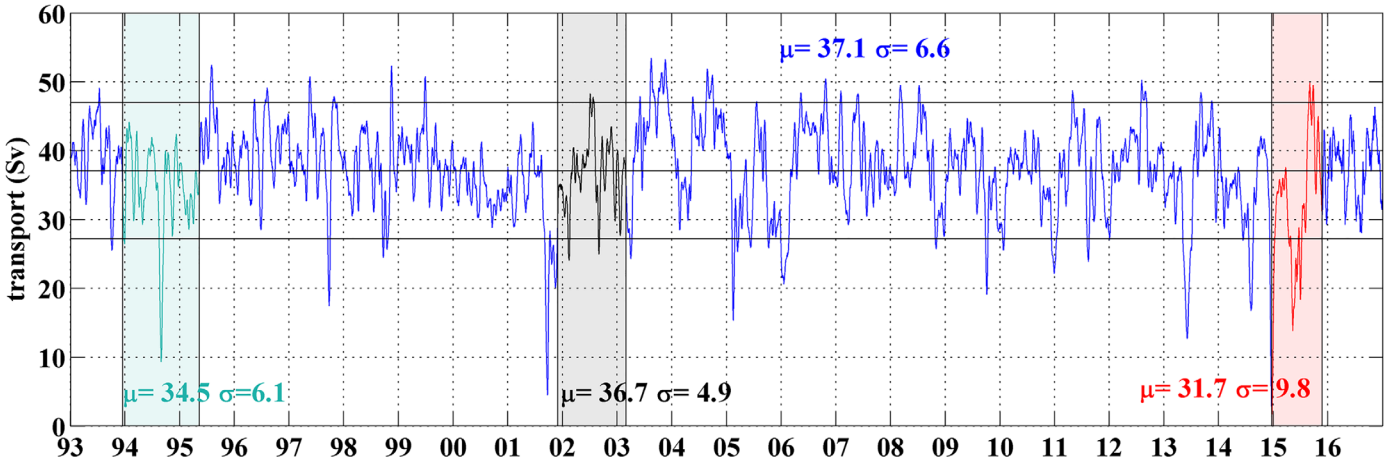

Figure 7. Volume transport (in Sv) in the upper 1,500 m computed with the LUT method using the fitted near-surface shear. The in situ measurement periods are indicated in colors. Horizontal lines indicate the mean and 1.5 standard deviation on each side of the mean.

The LUT transport estimates are now compared to existing time series. VP99b derived a transport time series using 256 days of in situ data (from December 1993 to August 1994) with a mean of 36.8 Sv and a standard deviation of 10.7 Sv. The means over the same period obtained with the three LUT differ from the one reported by VP99b by −0.9, −3.1, and +1.6 Sv for the fitted near-surface shear, the large near-surface shear and the zero near-surface shear, respectively. The transport difference between VP99b and SP09 over the same period is −5.2 Sv, VP99b being larger (Table 3). The four transport estimates derived from altimetry present reduced standard deviation (from 5.1 to 6.7 Sv) compared to VP99b (10.7 Sv; Table 3) as expected since the altimetry-derived velocities do not resolve high-frequency variations (Ferrari et al., 2017). The means of the LUT-derived transports computed over the 14 years examined in SP09 (1993–2007) are larger than the mean reported by SP09 (34.3 Sv) by 3.3 Sv (fitted shear), 6.1 Sv (zero shear), and 0.8 Sv (large shear). The SP09 parameters (Vm, A) derived in SP09 do not fit the in situ data as well as the LUT method (section 2.3) and provide consistently lower mean transport than any other estimate (VP99b or LUT derived; Table 3).

To better understand the differences in the statistics of the transport time series and for purpose of comparison, we recalculated the volume transport using equation (1) with the mean A(x,z) and $V_m(x,z)$ computed a posteriori from the LUT estimates (section 2.3, Figures 5 and 6). The a posteriori transport time series show correlations above 0.99 with the LUT transport time series. The root-mean-square (rms) of the difference between the transports (LUT and a posteriori with the classical method) are small 0.2, 0.3, and 0.4 Sv for the zero near-surface shear, the fitted shear, and the large near-surface shear hypotheses, respectively.

The difference in the mean (over the 24 years) between the LUT transport estimates (zero near-surface shear and large shear) is 5.2 Sv. It provides an upper bound on the error on the mean volume transport. Therefore, being conservative, we conclude that the mean transport of the MC over the 24 years is 37.1 ± 2.6 Sv and its standard deviation 6.6 ± 1.0 Sv. We chose to present the fitted shear volume transport times series shown in Figure 7.

Table 3
Statistics for MC Volume Transport

	SPO09			LUT fitted shear			LUT zero shear			LUT large shear		
	1993–1994 (256 days)	1993–2007 (15 years)	1993–2016 (24 years)	1993–1994 (256 days)	1993–2007 (15 years)	1993–2016 (24 years)	1993–1994 (256 days)	1993–2007 (15 years)	1993–2016 (24 years)	1993–1994 (256 days)	1993–2007 (15 years)	1993–2016 (24 years)
μ (Sv)	31.6	34.3	33.2	35.9	37.6	37.1	38.4	40.4	39.8	33.7	35.1	34.6
σ (Sv)	6.7	7.4	7.8	5.5	6.4	6.6	6.7	7.7	7.9	5.1	5.8	6.0

Note. Mean and standard deviation of the MC volume transport for the three LUT and the classic method for three different periods: from December 1993 to August 1994 (to compare with VP99b), from January 1993 to December 2007 (to compare with SP09), and from January 1993 to December 2016 (24 years of satellite altimetric data).

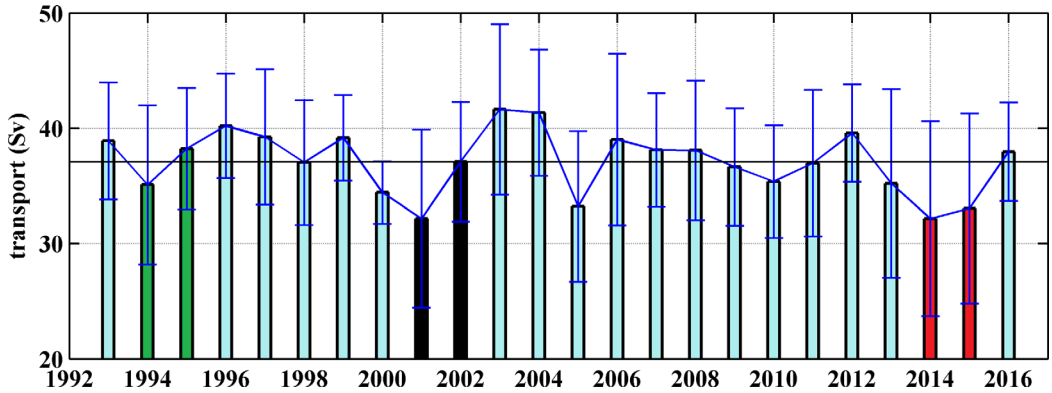

Figure 8. Yearly averages of the MC transport in the upper 1,500 m from January 1993 to December 2016. The standard deviation is shown by the blue line centered on each bar. Red, green, and black colored bars indicate in situ observation periods (1993–1995, 2001–2003, and 2014–2015, respectively). The black horizontal line marks the mean transport for 1993–2016.

3.2. Twenty-Four Yearlong MC Transport: General Statistics and Time Scales of Variations

The three in situ measurement periods present relatively weak MC transport with mean values of 34.5, 36.7, and 31.7 Sv compared to 37.1 Sv for 24 years (Figure 7). The last observation period (2014–2015) coincides with a very small mean value and a large standard deviation (9.8 Sv versus 6.6 Sv over 24 years; Figure 7). Annual means of volume transport and their annual standard deviations (Figure 8) show that years 2003

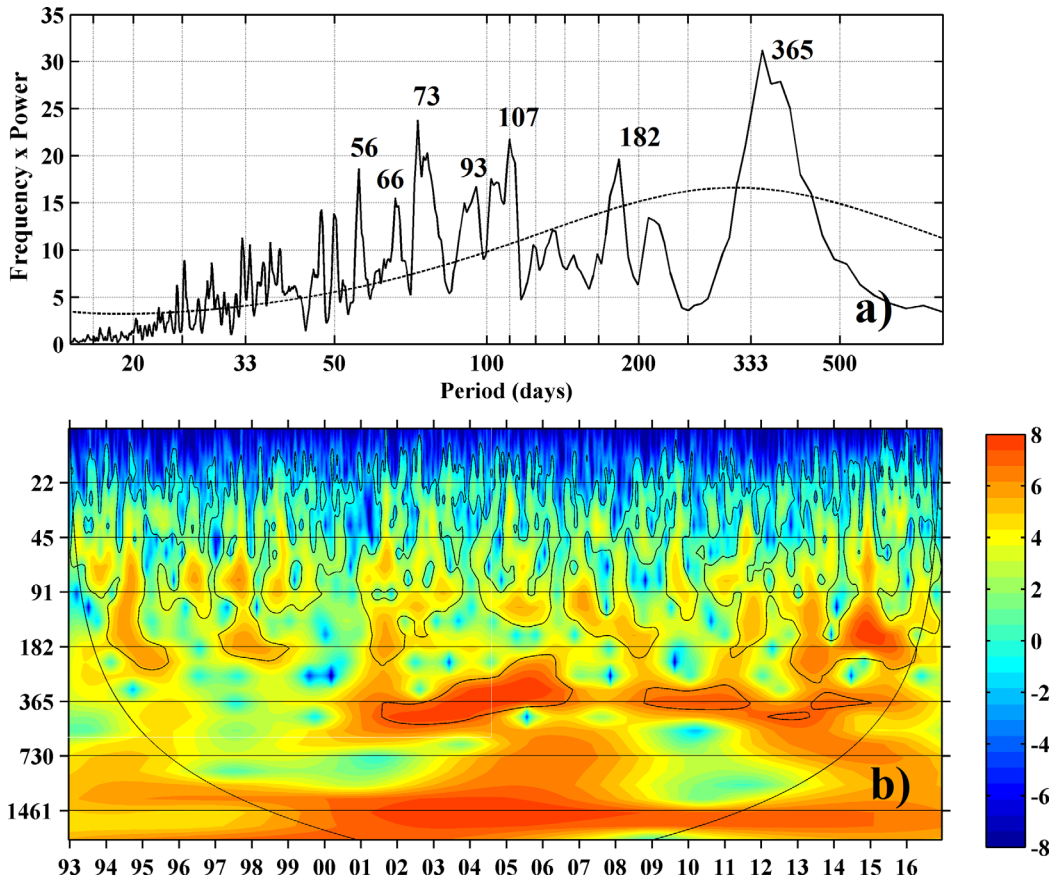

Figure 9. (a) Variance-preserving spectra of the MC transport by averaging over a group of five adjacent frequencies. The dotted line shows the 90% confidence level against the red noise background from a first-order autoregressive (ARI) process. (b) Corresponding wavelet transform amplitude shown in base 2 logarithm; *y* axis is the period in days and *x* axis is the time in years.

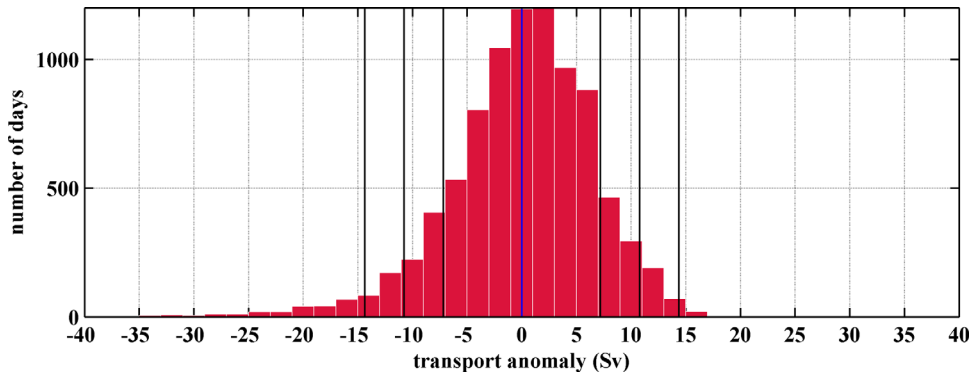

Figure 10. Distribution of the MC volume transport anomalies. *x* axis: volume transport anomaly values *y* axis number of days over 24 years. Black vertical lines mark the std, 1.5 std value, and 2 std values.

and 2004 are characterized by a large annual mean (41.6 and 41.3 Sv, respectively, standard deviation of 7.4 and 5.5 Sv) and 2014 by the smallest annual mean (32.1 Sv) and largest standard deviation (8.4 Sv). The yearly averages of volume transport suggest a low-frequency modulation with a time scale of several years. The volume transport time series does not show any significant trend.

The correlation of the cross-track satellite surface velocity anomaly at each point of the section with the transport time series reaches a maximum of 0.95 in the vicinity of the mooring 9M3, around 62 km (bathymetry: 1,500 m). This implies that the variability of the MC transport can be properly monitored based on the surface velocity anomaly variability at this point.

The transport time series cannot resolve variations with periods shorter than 20 days. The variance-preserving spectrum of the transport time series (Figure 9a) shows significant peaks with elevated energy at periods between 30 and 110 days. This period band is probably associated with baroclinic coastal trapped waves propagating along the edge of the Patagonian shelf (Vivier et al., 2001). Other salient peaks above the 95% confidence level are found at the semiannual and annual periods, the annual being the largest peak. The spectral content of the transport time series is modulated in time as shown in the wavelet transform amplitude (Figure 9b) with variable relative energy around the 70 day period, the semiannual and annual periods. The energy around 70 day period is larger during the first 6 years of the time series. There is no energy at the annual period before 2001 and a significant amount after 2001. The energy at the semiannual period is patchy, significant before 2001 and after 2010 (Figure 9b).

The MC transport time series (Figure 7) also shows important short-term variations with several strong apparently aperiodic peaks during which the MC transport decreases by more than 40% with respect to the mean in less than a month. In three occasions, the MC transport even reduces to less than 10 Sv (around 6 September 1994, 26 September 2001, and 1 January 2015, Figure 7). In fact, due to these events, the distribution of the MC volume transport anomalies shows a remarkable asymmetry (Figure 10). The Fisher-Pearson coefficient of skewness is -0.80 corresponding to a long left tail (–29 Sv) relative to the right tail ($+17$ Sv): negative transport anomalies are larger than positive transport anomalies.

4. Variations of MC Volume Transport

4.1. Extremes Events: Maxima and Minima of the MC Transport

An event is considered extreme when its deviation from the mean is larger than ± 1.5 standard deviation. This criterion selects 25 minima and 23 maxima. The mean duration of extreme events, whether positive or negative, is about 22 days. The SLA composite corresponding to the positive events (Figure 11a) shows a tripole of anomalies in the 40–42°S latitudinal band. The tripole comprises a cyclonic anomaly (<-15 cm) centered at 55°W and 41°S impinging on the offshore side of mooring section, a positive elongated anomaly (>15 cm, 53°W, 41°S) reinforcing the BC overshoot and a strong negative anomaly further offshore (<-30 cm, 51°W, 40.5°S). In contrast, the composite of SLA maps corresponding to transport minima (Figure 11b) shows a tripole of the opposite sign with a strong anticyclonic anomaly (>30 cm) next to the mooring section, a strong negative anomaly (<-30 cm, 52°W, 41°S), and a positive anomaly (>20 cm, 49°W,

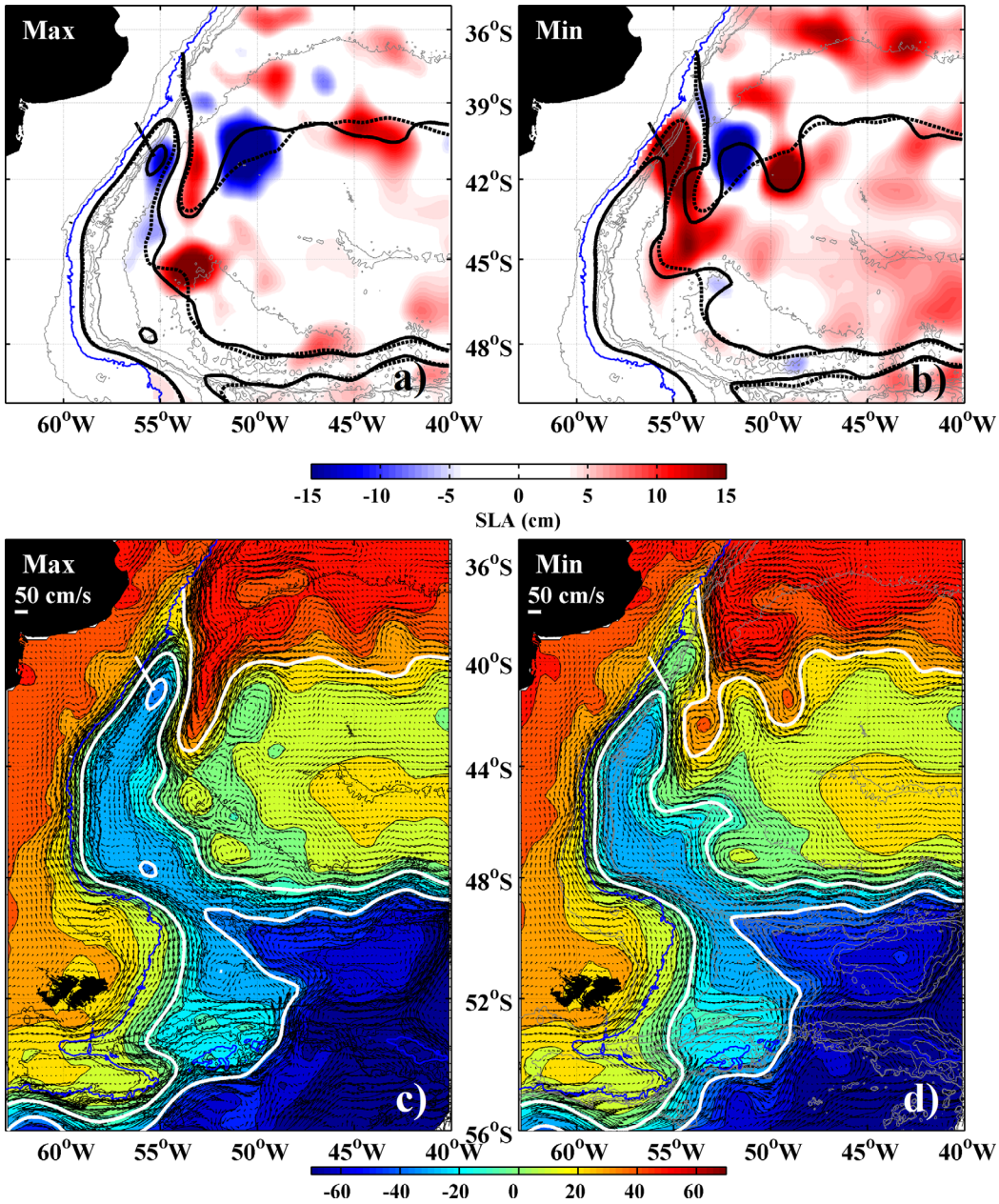

Figure 11. (a, b) SLA and (c, d) ADT composites (cm/s) for the 25 minima and for the 23 maxima in volume transport. Associated surface geostrophic velocities in cm/s are shown on the ADT. Black (white) solid contours in Figures 11a and 11b. (Figures 11c and 11d) indicate the SAF, BCF, and PF position during extrema. Black (white) dashed contours in Figures 11a and 11b (Figures 11c and Figure 11d) mark the mean position of the SAF, BCF, and PF during the whole altimetric period. The fronts are defined as in Figure 1. The 1,000 m isobath is indicated with a blue contour. Isobaths are the same as in Figure 1. The black (white) line in Figures 11a and 11b (Figures 11c and 11d) indicates the position of Jason track #26.

41.5°S). As transport minima are more extreme than maxima, the SLA amplitude next to the mooring section is logically larger in the case of transport minima. In either case no anomaly signal is observed along the continental slope that is along the path of the MC.

The surface circulation associated with MC transport maxima (Figure 11c) indicates that during transport maxima the SAF extends north past the mooring section and reaches the same location as the record length mean SAF. The only difference with the mean SAF location is found offshore as the southward path of the SAF is pushed eastward by the negative sea level anomalies between 40 and 45°S at 55°W (Figure

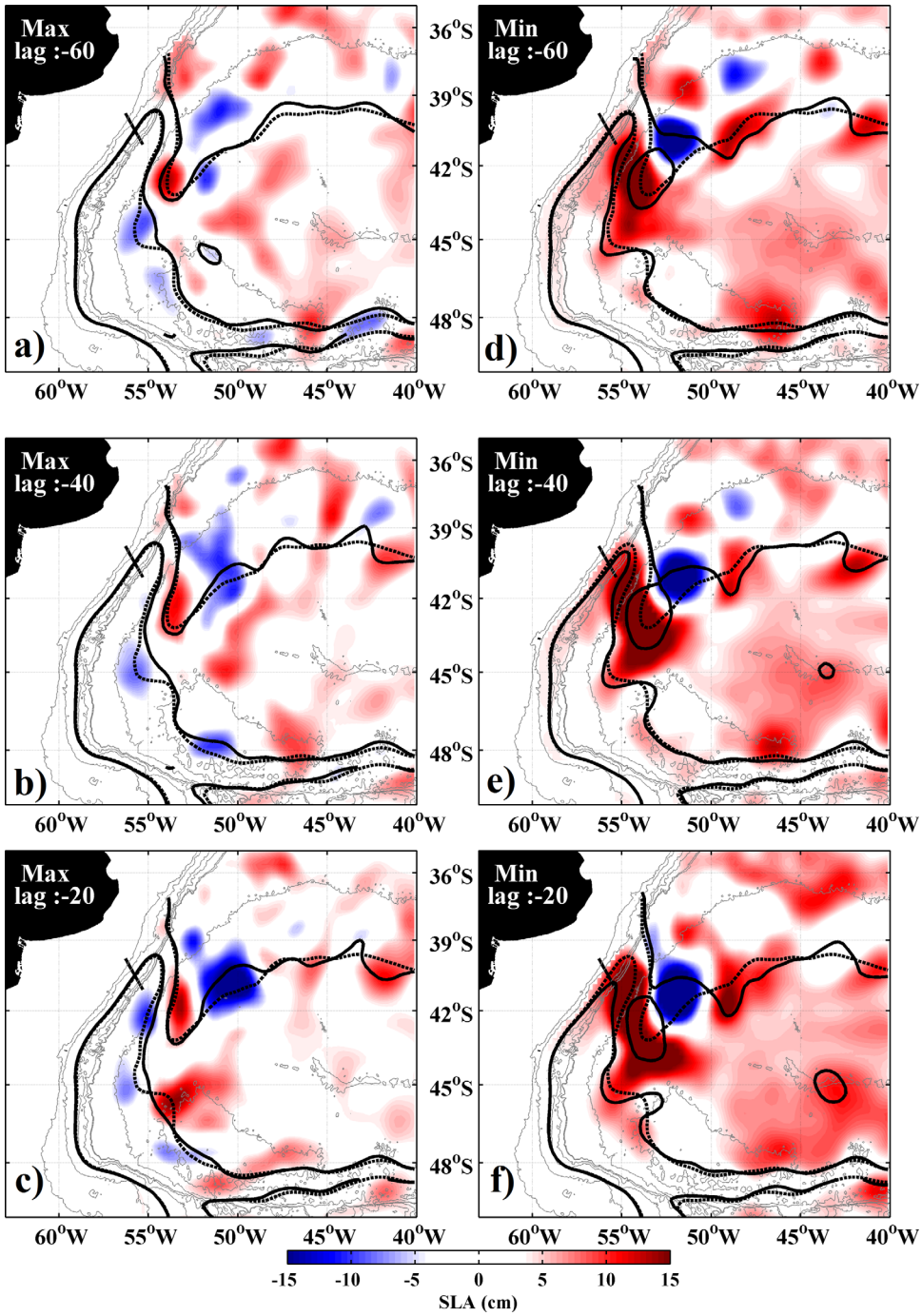

Figure 12. Lagged composites of SLA for (a–c) maxima and (d–f) minima (Lag 0 day are on Figures 10a and 10b). Color scale in cm. Isobaths are the same as in Figure 1. Solid contours indicate the corresponding front locations (SAF, BCF, and PF) and dashed contours their mean positions over 1993–2016. The black line indicates the position of Jason track #26.

11a). In contrast, the surface circulation corresponding to transport minima (Figure 11d) indicates that the SAF loops southward south of the mooring section and that the MC splits into two branches at 41°S: one, offshore, performs a cyclonic loop at 41°S and then flows adjacent to the BC overshoot while the second inshore branch continues flowing northward along the 1,000 m isobath, up to 39°S where it meets the Brazil Current. It is remarkable that the separation of the Brazil Current Front (BCF) from the slope (the 1,000 m isobath) occurs at a similar latitude (around 36°S) both during transport minima or maxima, and that the overshoot is more intense during maxima than during minima (Figures 11c and 11d).

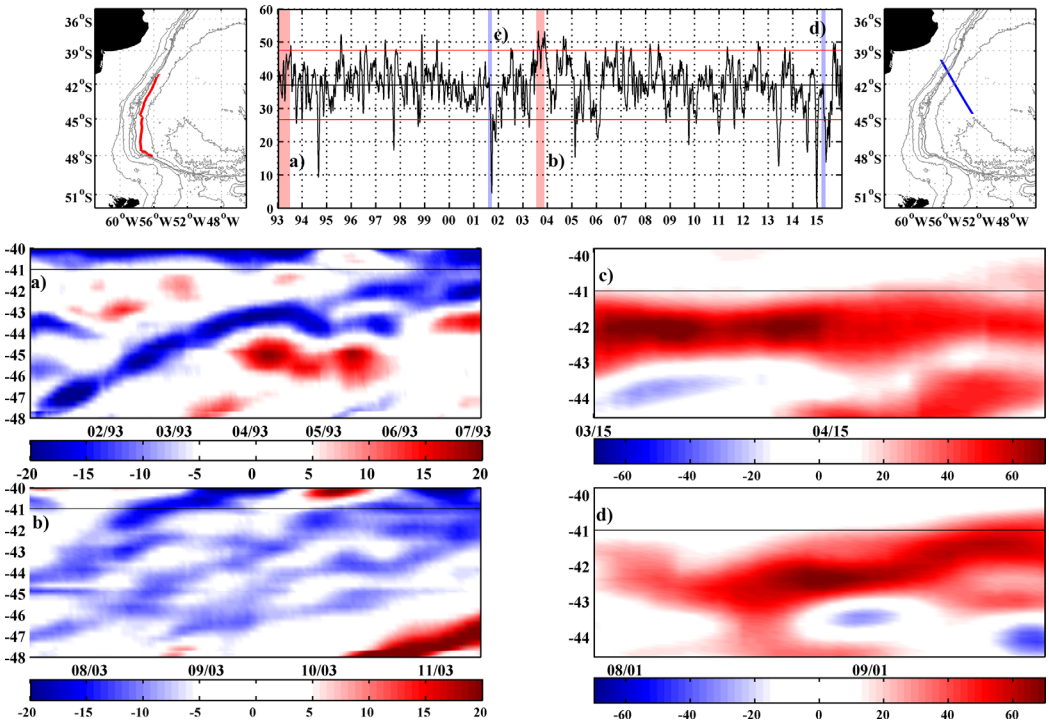

Figure 13. (a, b) Hovmöller diagrams of SLA (along the 4,000 m isobath colored in red in the map on the top left) corresponding to the periods indicated in red in the transport time series (top middle). Those periods precede a transport maximum. They show northward propagation of negative anomalies. The mean propagation speed is about 6 km/d. Note that in Figure 13b, there are three successive anomalies corresponding to the three maxima occurring during that period (August–November 2003). (c, d) Hovmöller diagrams of SLA along Jason track #26 (blue line in the map in the top right) corresponding to periods indicated in blue in the transport times series. Those periods precede transport minima. The propagation speed is small and variable about 2–3 km/d. Note the different scales in SLA, in *x* and *y* axes of the Hovmöller diagrams for maxima and minima. The *x* axis ticks are expressed as mm/yy.

To further investigate the nature and possible cause of these circulation anomalies, we examine lagged composites for transport maxima and minima.

4.2. Lagged Composites for Maxima and Minima of the MC Transport

Lagged composites for transport maxima (Figures 12a–12c) show the presence of cyclonic anomalies between 48°S and 50°W over the 4,000–5,000 m isobath, west of the Malvinas Return Current (MRC). The northward displacement of the cyclonic anomalies with time could be indicative of a north-northwest propagation of cyclonic anomalies. The lagged composites (Figure 12) provide a blurred illustration of the propagation as each is a mean of ~24 events (23 maxima and 25 minima) with different intensities. However, propagations are clear if each extremum is considered separately. To illustrate the propagation we present two SLA Hovmöller diagrams along the 4,000 m isobath for two time periods that precede transport maxima (Figures 13a and 13b). The Hovmöller diagram clearly shows a northward propagation of negative SLA along the 4,000 m isobath, resulting in a maximum in MC transport at 41°S. The propagation speed is about 6 km/d. This is the same order of magnitude as mesoscale eddy northward propagation speed along the 4,000 m isobath estimated by Fu (2006) and Mason et al. (2017). The cyclonic anomalies are traced back to the south of the Argentine Basin. When (and if) the cyclonic anomalies reach 41°S, they increase the MC transport on the slope through a local recirculation cell. In some cases, the cyclonic anomalies appeared to be shed from the PF. The shedding occurs as the PF exits the Malvinas Plateau (48°S and 50°W) and turns eastward following the Malvinas Escarpment. The diverging isobaths in that region favor the development of instabilities and current splitting (Arhan et al., 2002). As the PF continues its eastward path, it meanders along the Malvinas Escarpment and sporadic eddies are shed as well (Fu, 2006, 2009).

Lagged composites for transport minima (Figures 12d–12f) show a large positive sea level anomaly breaking off the BC overshoot that seems to propagate northwestward toward the continental slope. The SAF

retreats south as the positive sea level anomaly reaches the slope. Hovmöller diagrams of SLA along a section parallel to the track for two time periods that precede transport minima (Figures 13c and 13d) suggest a slow northwestward propagation of large positive SLA toward the slope. The propagation speed of the positive anomaly is slow (about 2–3 and 1 km/d), in agreement with mesoscale westward propagation speed in the vicinity of the BMC estimates from Fu (2006) and Mason et al. (2017). Overall, it is difficult to trace anomalies back further in space and time in this extremely high eddy kinetic energy environment, and the development of the positive anomaly may differ from one transport minimum to the other.

In the following section, we examine statistical relationships (not only extrema) between the transport variations and sea level anomalies over the Southwestern Atlantic Ocean.

4.3. MC Transport Variations and SLA Over the Southwestern Atlantic Ocean

The SLA field over the Southwest Atlantic is regressed onto the 24 yearlong normalized transport time series at different lags. The statistical significance is tested using a two-side Student's test. As the transport

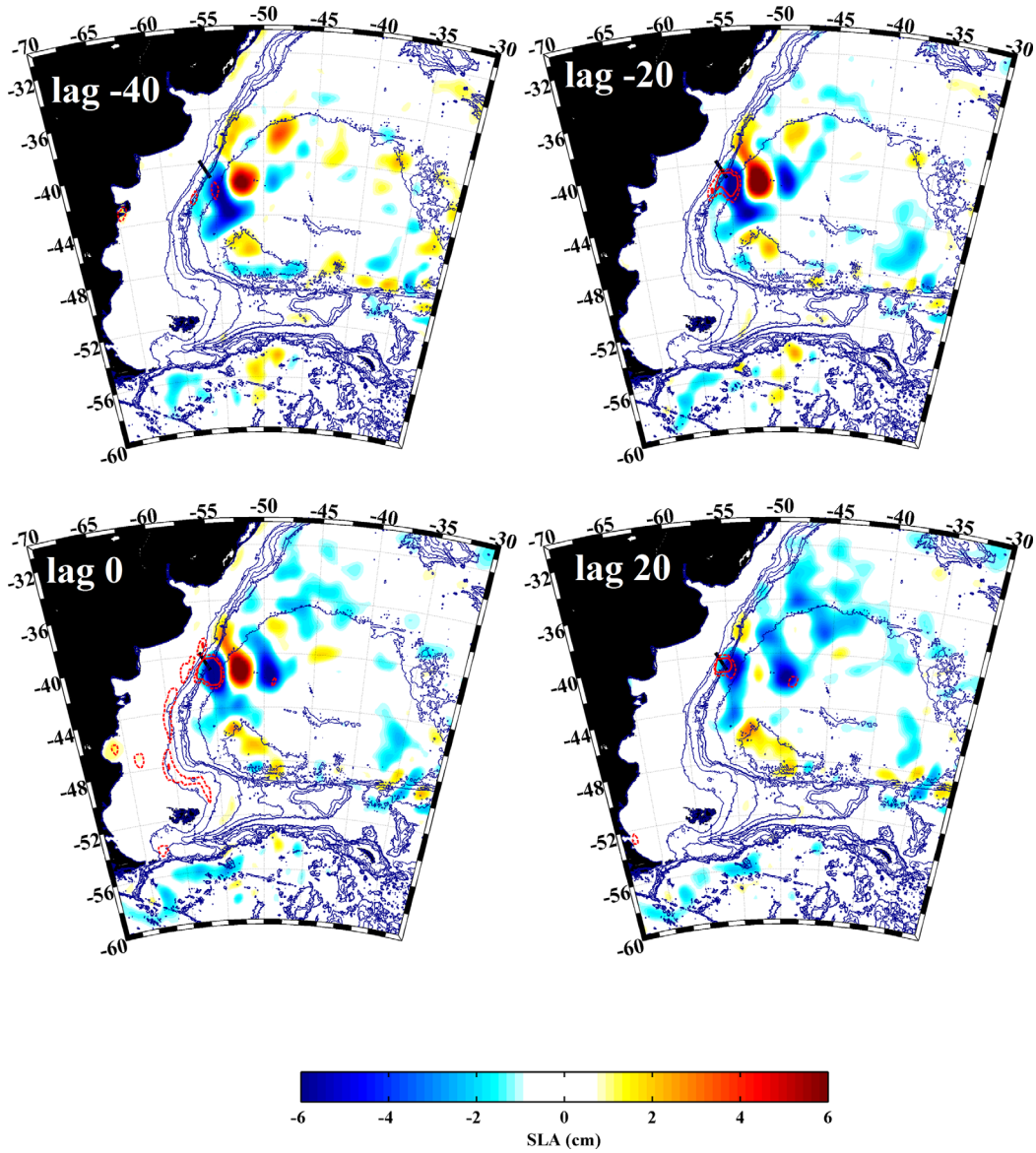

Figure 14. Regression of SLA on the time series of the MC volume transport normalized by the standard deviation. Lags at −40, −20, 0, and +20 days are shown. Solid red contours represent the correlation at 90% confidence level; dashed red contours represent the 95% confidence level. Color scale is SLA in centimeters. Isobaths are the same as in Figure 1.

time series is not stationary (the spectral content is modulated in time) regressions were also performed on four 6 yearlong portions of the time series with more homogeneous spectral content. Similar results are obtained with each 6 year portion of time series (not shown). SLA regressions at lag 0 day always feature the same patterns (Figure 14): a robust SLA tripole adjacent to the section in the latitude range 40°S–42°S and significant regressions (above the 95 or 99% confidence level) along the continental slope (with a weak positive SLA signal of about 2 cm) and in the negative parts of the tripole. The significant regression patterns along the slope observed at lag 0 (and only at lags less than 15 days) are possibly associated with a train of fast baroclinic coastal trapped waves propagating along the edge of the Patagonian shelf (Artana et al., 2016; Vivier et al., 2001). The rapid propagation speed of these waves, of the order of a few m/s, is not resolved in the altimetry maps (Koenig et al., 2016). Consequently, these waves appeared aliased in the regression maps (Artana et al., 2016). The tripole observed at lag 0 in the vicinity of the mooring array corresponds to a situation where a strong cyclonic circulation is established in the northern part of the MC and an anticyclonic circulation reinforces the BC overshoot. The pattern is qualitatively similar to the transport maxima composite shown in Figure 11c.

Significant regressions (above the 95 or 99% confidence level) are observed from lag −40 to +20 days in the negative SLA adjacent to the mooring line (Figure 14). The SLA tripole is quasi-stationary and builds up in amplitude as lag decreases. At lag 0, the negative and positive anomalies reach −10 cm and +10 cm, respectively. After lag 0, the SLA patches decrease in amplitude and after lag 30 no significant correlations are found. Significant regressions are confined to the vicinity of the moorings. Apart from the signal possibly corresponding to coastal trapped waves, there is no signal along the MC path at any lag, suggesting that variations of the MC transport at 41°S are locally forced and disconnected from upstream variability. The temporal scale associated with this regression is annual as a positive anomaly is observed on the mooring section at lag −180 and +180 days.

The observed significant regression is a robust pattern in the whole altimetric period. It also emerged in regression maps produced over the period 1993–2001 (dominated by the semiannual period, Figure 9) and over the period 2001–2016 (dominated by the annual period, Figure 9). While tracking back the significant regression in these maps, we identified three westward paths of SLA propagation converging toward the mooring line and potentially feeding the tripole anomaly described above. The first one is zonal path between 38°S and 42°S with a wave-train-like SLA patches slowly propagating westward against the mean flow. The second path is southwestward along the slope from 35°S in the same direction as the BC mean flow. The third path is northwestward starting from the deepest part of the Argentine Basin (47°S, 52°W) and against the mean flow. The propagations against the mean flow are very slow. Anomalies build up in intensity as they are blocked by the continental slope. Searching for the origin of the anomalies is difficult and beyond the scope of this work.

5. Summary and Conclusion

We computed a 24 yearlong time series of the Malvinas Current transport in the upper 1,500 m at 41°S combining in situ current velocity time series and satellite altimetry data. Each in situ data set was about a year long and altogether the three roughly 10 years apart observation periods provided information across the continental slope.

We used the new LUT method recently developed by Koenig et al. (2014) and explored three types of shear encompassing a wide range (no shear, fitted, and large shears) to estimate the uncertainty attached to the lack of information on the velocity shear in the upper 300 m of the water column. The no shear and large shear hypotheses represent two extreme cases. The LUT-reconstructed velocities accurately corresponded to the 20 day low-passed in situ velocities from the three periods. Although the three types of upper shear led to significantly different mean surface velocity estimates (difference up to 8 cm/s in the core of the MC), the resulting transport time series were highly correlated with each other (0.99) with root-mean-square differences around 1 Sv, the zero-shear hypothesis providing the largest std (7.9 Sv versus 6.0 Sv). The uncertainty on the mean transport estimate is about 2.6 Sv (less than 10% of the volume transport mean). The mean of the transport time series over 24 years is 37.1 ± 2.6 Sv and the standard deviation 6.6 ± 1 Sv. The new transport time series agrees with the transport derived from in situ measurements by VP99b and is 3.9 Sv larger than the mean transport of SP09. Since 1993, annual mean transports varied from 32 to 41 Sv and the three measurement periods

corresponded to periods of relatively low annual mean transport. In general, large annual std are associated with small mean transports. There is no significant trend in the MC volume transport.

The distribution of the MC volume transport anomalies is asymmetric with a negative skewness as transport anomalies are larger during minima than during maxima. Lagged composites of SLA for transport minima or maxima showed no anomaly signal along the path of the MC on the continental slope, suggesting that transport anomalies near the northernmost reach of the MC are not derived from upstream sources. Several transport maxima resulted from cyclonic anomalies that propagated from the south following the 4,000–5,000 m isobaths and locally reinforced the circulation on the slope when they reach 41°S. Sporadic cold cyclonic eddies with a 10–40 day persistence have been observed in the offshore edge of the MC close to the Confluence region (Garzoli & Garraffo, 1989). The cyclonic sea level anomalies were traced back to the south of the Argentine Basin and appeared to detach from the PF either as the PF turns east at the exit of the Malvinas Plateau or further east from PF meanders along the Malvinas Escarpment. These eddy pathways are described in Fu (2006). During MC transport maxima, the SAF location remained basically close to its mean location (up to 39.5°S). In contrast, during transport minima, the SAF was displaced southward, back on the mooring line in extreme cases, as large and intense (>30 cm) positive sea level anomalies shed by the overshoot managed to propagate westward onto the slope. The sea level anomaly propagation velocities (6 km/d along a northwest path closely following the 4,000 m isobaths in the southern Argentine Basin leading to transport maxima and 2–3 km/d westward in the highest EKE region of the Confluence about 41°S–43°S leading to transport minima) are similar to estimates from Fu (2006) and Mason et al. (2017). Regardless of the sign of the intense MC transport anomalies, the separation of the BCF from the 1,000 m isobaths remained at the same location, in agreement with Saraceno et al. (2004). The major differences in the BCF were observed offshore as the BC overshoot weakened during MC transport minima and intensified during maxima.

The link between the volume transport of the MC and the position of the SAF and BCF is not straightforward. In a companion paper, Ferrari et al. (2017) identified two modes of variations of SLA over the Brazil-Malvinas Confluence. The first one is related with a latitudinal migration of the SAF, that is the northward penetration of the MC, and the second with a longitudinal displacement of the Brazil Current overshoot. Neither of the associated EOFs time series are significantly correlated with the transport time series suggesting that the MC transport variations are not driving the variability.

SLA fields regressed onto normalized transport time series showed that changes in the MC volume transport at 41°S, apart from coastal trapped waves bore no correlation with upstream conditions on the continental slope. A large fraction of the variability of the MC transport at 41°S appeared to be controlled by anomalies propagating over the Argentine Basin and converging at 41°S. Three main propagation paths were identified while performing the regression on portions of the time series with homogenous spectral content: a southwestward propagation from the BC in the same direction as the mean flow, a very slow westward propagation in the latitudinal band 39°S–42°S against the mean flow and a northwestward propagation from the deep abyssal plain against mean flow. Anomaly patterns identified in the analysis of transport minima and maxima were blurred in the regression analysis.

The spectral content of the MC transport showed significant energy in the range 30–110 day range, and in the semiannual and annual periods. As noticed by SP09, the MC transport time series is not stationary; rather its spectral content evolves with time. Baroclinic coastal trapped waves observed by Vivier et al (2001) contribute to the energy content with a period of 30–110 days. The 70 day period was particularly energetic during the first 6 years of the time series (1993–1998). Years 1993–1998 and from 2010 to 2016 were characterized by a strong semiannual variability. In contrast, the period between 1999 and 2010 was mostly dominated by the annual variability. Identifying the main processes that modulate the spectral content of the MC transport time series is a difficult task due to the complex dynamics of the region. Long-term variations are beyond the scope of this work since the satellite altimetric record length is yet too short to study the variability of the MC transport at low frequencies.

Acknowledgments
The authors are deeply grateful to the CNES (Centre National d'Etudes Spatiales) for the constant support. This study is a contribution to EUMETSAT/CNES DSP/OT/12-2118. We acknowledge support from the MINCYT-ECOS-Sud A14U0 projects ECOS-Sud program in facilitating scientific exchanges between Argentina and France. Camila Artana and Zoe Koenig are funded under PhD scholarships from Université Pierre et Marie Curie and Sorbonne Université. The satellite data are available at Copernicus Marine Environment monitoring service (CMEMS; http://marine.copernicus.eu/) and the in situ data are available at SEANOE (www.seanoe.org; cf., Provost et al., 2017a, 2017b; Saraceno et al., 2017). We are grateful to the Editor, Don Chambers, to an anonymous reviewer and to Josep Lluís Pelegrí for a number of constructive comments and suggestions.

References

Acha, E. M., Mianzan, H. W., Guerrero, R. A., Favero, M., & Bava, J. (2004). Marine fronts at the continental shelves of austral South America: Physical and ecological processes. *Journal of Marine Systems*, *44*(1–2), 83–105. https://doi.org/10.1016/j.jmarsys.2003.09.005

Arhan, M., Carton, X., Piola, A., & Zenk, W. (2002). Deep lenses of circumpolar water in the Argentine Basin. *Journal of Geophysical Research*, *107*(C1). https://doi.org/10.1029/2001JC000963

Artana, C., Ferrari, R., Koenig, Z., Saraceno, M., Piola, A. R., & Provost, C. (2016). Malvinas Current variability from Argo floats and satellite altimetry. *Journal of Geophysical Research: Oceans*, *121*, 4854–4872. https://doi.org/10.1002/2016JC011889

Carranza, M. M., Gille, S. T., Piola, A. R., Charo, M., & Romero, S. I. (2017). Wind modulation of upwelling at the shelf-break front off Patagonia: Observational evidence. *Journal of Geophysical Research: Oceans*, *122*, 2401–2421. https://doi.org/10.1002/2016JC012059

Ferrari, R., Artana, C., Saraceno, M., Piola, A. R., & Provost, C. (2017). Satellite altimetry and current-meter velocities in the Malvinas Current at 41°S: Comparisons and modes of variations. *Journal of Geophysical Research: Oceans*, *122*, 9572–9590. https://doi.org/10.1002/2017JC013340

Fu, L.-L. (2006). Pathways of eddies in the South Atlantic Ocean revealed from satellite altimeter observations. *Geophysical Research Letters*, *33*, L14610. https://doi.org/10.1029/2006GL026245

Fu, L.-L. (2009). Pattern and velocity of propagation of the global ocean eddy variability. *Journal of Geophysical Research: Oceans*, *114*, C11017. http://doi.org/10.1029/2009JC005349

Garzoli, S. L., & Garraffo, Z. (1989). Transports, frontal motions and eddies at the Brazil-Malvinas Currents Confluence. *Deep Sea Research Part A: Oceanographic Research Papers*, *36*(5), 681–703.

Garzoli, S. L., & Giulivi, C. (1994). What forces the variability of the Southwestern Atlantic Boundary Currents? *Deep-Sea Research Part I: Oceanographic Research Papers*, *41*, 1527–1550. https://doi.org/10.1016/0967-0637(94)90059-0

Koenig, Z., Provost, C., Ferrari, R., Sennéchael, N., & Rio, M. H. (2014). Volume transport of the Antarctic Circumpolar Current: Production and validation of a 20 year long time series obtained from in situ and satellite observations. *Journal of Geophysical Research: Oceans*, *119*, 5407–5433. https://doi.org/10.1002/2014JC009966

Koenig, Z., Provost, C., Park, Y.-H., Ferrari, R., & Sennéchael, N. (2016). Anatomy of the Antarctic Circumpolar Current volume transports through Drake Passage. *Journal of Geophysical Research: Oceans*, *121*, 2572–2595. https://doi.org/10.1002/2015JC011436

Mason, E., Pascual, A., Gaube, P., Ruiz, S., Pelegrí, J. L., & Delepoulle, A. (2017). Subregional characterization of mesoscale eddies across the Brazil-Malvinas Confluence. *Journal of Geophysical Research: Oceans*, *122*, 3329–3357. https://doi.org/10.1002/2016JC012611

Piola, A. R., Franco, B. C., Palma, E. D., & Saraceno, M. (2013). Multiple jets in the Malvinas Current. *Journal of Geophysical Research: Oceans*, *118*, 2107–2117. https://doi.org/10.1002/jgrc.20170

Provost, C., Lanoisellé, J., Kartavtseff, A., Spadone, A., Artana, C., & Durand, I. (2017b). *Malvinas Current 2001–2003: Mooring velocities*. SEANOE. https://doi.org/10.17882/51479

Provost, C., Lanoiselle, J., Kartavtseff, A., Vivier, F., Artana, C., & Durand, I. (2017a). *Malvinas Current 1993–1995: Mooring velocities*. SEANOE. https://doi.org/10.17882/51483

Pujol, M.-I., Faugère, Y., Taburet, G., Dupuy, S., Pelloquin, C., Ablain, M., & Picot, N. (2016). DUACS DT2014: The new multi-mission altimeter data set reprocessed over 20 years. *Ocean Science*, *12*, 1067–1090. https://doi.org/10.5194/os-12-1067-2016

Rio, M.-H., Mulet, S., & Picot, N. (2013). *New global Mean Dynamic Topography from a GOCE geoid model, altimeter measurements and oceanographic in situ data*. Paper presented at ESA Living Planet Symposium, Edinburg, TX.

Romero, S. L., Piola, A. R., Charo, M., & García, C. E. (2006). Chlorophyll-*a* variability off Patagonia based on SeaWiFS data. *Journal of Geophysical Research*, *111*, C05021. https://doi.org/10.1029/2005JC003244

Saraceno, M., Guerrero, R., Piola, A. R., Provost, C., Perault, F., Ferrari, R., . . . Artana, C. (2017). *Malvinas Current 2014–2015: Mooring velocities*. SEANOE. https://doi.org/10.17882/51492

Saraceno, M., Provost, C., Piola, A. R., Bava, J., & Gagliardini, A. (2004). Brazil Malvinas Frontal System as seen from 9 years of advanced very high resolution radiometer data. *Journal of Geophysical Research*, *109*, C05027. https://doi.org/10.1029/2003JC002127

Smith, W. H. F., & Sandwell, D. T. (1994). Bathymetric prediction from dense satellite altimetry and sparse shipboard bathymetry. *Journal of Geophysical Research*, *99*, 21803–21824.

Spadone, A., & Provost, C. (2009). Variations in the Malvinas Current volume transport since October 1992. *Journal of Geophysical Research*, *114*, C02002. https://doi.org/10.1029/2008JC004882

Valla, D., & Piola, A. R. (2015). Evidence of upwelling events at the northern Patagonian shelf break. *Journal of Geophysical Research: Oceans*, *120*, 7635–7656. https://doi.org/10.1002/2015JC011002

Vivier, F., & Provost, C. (1999a). Direct velocity measurements in the Malvinas Current. *Journal of Geophysical Research*, *104*, 21083–21103. https://doi.org/10.1029/1999JC900163

Vivier, F., & Provost, C. (1999b). Volume transport of the Malvinas Current: Can the flow be monitored by TOPEX/Poseidon? *Journal of Geophysical Research*, *104*, 21105–21122. https://doi.org/10.1029/1999JC900056

Vivier, F., Provost, C., & Meredith, M. (2001). Remote and local forcing in the Brazil Malvinas Region. *Journal of Physical Oceanography*, *31*, https://doi.org/10.1175/1520-0485